A dynamic model of polyethylene damage in dry total hip arthroplasties

wear and creep

Renani, Ehsan Askari; Andersen, Michael Skipper

A dynamic model of polyethylene damage in dry total hip arthroplasties: wear and creep

Ehsan Askari[1]

Department of Materials and Production, Aalborg University, Aalborg 9220, Denmark

e-mail: ehsanaskary@gmail.com

Michael S. Andersen

Department of Materials and Production, Aalborg University, Aalborg 9220, Denmark

e-mail: msa@mp.aau.dk

ABSTRACT

The creep and wear of ultra-high-weight polyethylene hip prostheses under physiological conditions are studied in the present research work. A fully integrated contact-coupled dynamic model based upon multibody dynamics methodology is developed, allowing the evaluation of not only sliding distance, but also contact mechanics as well as cross-shear effects and both average pressure and in-service duration associated with the creep phenomenon. In vivo forces and motions of hip joint are used as input for the dynamic simulation, which result in more realistic contact point trajectory and contact pressure, and consequently wear and creep compared to simplified inputs. The analysis also takes into account inertia forces due to hip motion, tribological properties of bearing bodies, and energy loss owing to contact-impact events. The principal molecular orientation (PMO) of the polyethylene cup is determined through an iterative algorithm and dynamic outcomes. Archard's wear law is also integrated into the multibody dynamics model in order for wear prediction in hip implants. Creep, besides wear, is attributed to polyethylene damage, which is investigated by implementing a creep model extracted from experimental data. The model is validated as compared to clinical data and numerical results available by previous published studies. It is shown that creep plays a significant role in hip damage along with wear both of which can be influenced by hip parameters, e.g. hip and clearance sizes. Moreover, the creep mechanism according to creep experiment is discussed and contributing factors to the wear phenomenon are analyzed throughout this study.

Keyword: Multibody dynamics; tribology; total hip replacement; Contact mechanics

---

[1] *Corresponding author.*

E-mail address: ehsanaskary@gmail.com (E. Askari)

INTRODUCTION

More than 2 million hip replacements are performed per annum worldwide, which will undergo a twofold increase by 2020 due to an aging population [1]. The 2014 Canadian Joint Replacement Registry also reported that the number of total hip replacements has increased by 16.5% during the last five years [2]. Moreover, the demographics indicate an increase in number of younger patients (45-64 years) and hence, hip arthroplasties are now required to last over 30 years [3], with greater functional demands. Since the early artificial hip joints, around the 1960s, the most popular and used combination of hip prostheses has been a metal/ceramic femoral head against a polyethylene cup [4-5]. Ultra-high molecular weight polyethylene (UHMWPE) has shown a superior mechanical toughness and wear resistance compared to most other polymers, having commonly been the material of choice in both total knee and hip replacements [6]. One of key factors in the primary failure of artificial hip joints is wear, which can influence the performance and life expectancy of an implant [7]. Owing to the articulation of hip components, UHMWPE wear debris are generated, entering the periprosthetic tissues and stimulating bone resorption that may eventually lead to the implant loosening [8-9]. The consequence of wear may be that the patient must undergo revision surgery to replace the original implants. This is clearly an undesired outcome due to the hardship it imposes on the patient and health budget.

While clinical studies produce actual wear data of artificial hip joints [10], implant retrievals are rarely analyzed as they involve large-scale and long-

term follow-up hip replacements studies. In addition, patient factors such as weight and activity levels result in many confounding factors. Preclinical laboratory wear tests by means of hip simulators are vital for new implant designs and materials [11], although such tests are costly and time-consuming. Computational wear simulations are an alternative to bypass these disadvantages, which is faster and cheaper in providing predictions of wear and in investigating the effect of hip prosthesis design parameters on wear [12]. Therefore, a significant effort has been placed on advancing computational wear models [13-23]. Numerical wear simulation requires knowledge of the sliding distance, contact pressure, and tribological data, namely the wear factor [24].

The contact pressure generated because of colliding hip parts can be computationally determined by means of the finite element method [24], boundary element method [25], simplified elastic models [26], and the Hertz contact model [14, 27]. Each has its advantages and disadvantages in terms of accuracy and numerical efficiency; for instance, it is well-known that the finite element method provides accurate results, but it is very time-consuming [28]. The second contributing factor is the sliding distance that is attributed to the relative motion of colliding bodies, e.g. the femoral head and the acetabular cup, which is acquired by the dynamic simulation of the hip implant [29]. The slide track is a crucial parameter to evaluate the wear, since any variation in the track shape can cause a notable difference in the wear rate [30-32]. This trajectory is commonly obtained from the physiological data of either rotational movement or loading [19, 33-35]. Therefore, the resultant simplified contact

3

point trajectory does not account for nonlinear characteristics of the relative motion between bearing components (e.g. stick-slip and sliding), impact-contact, inertia forces, friction-induced vibration, damping effect of the plastic cup, etc. For instance, friction-induced vibration affects the contact point trajectory, causing wear rates in ceramic hip couples to increase significantly, but a simplified sliding track cannot address this phenomenon [27, 36].

The wear factor is dependent on the system parameters, e.g. the geometric and material properties of colliding bodies; friction and lubrication; and the wettability of materials involved [23, 37]. It has been obtained either from hip simulator or from pin-on-disk tests [38-39]. In contrast to either ceramic or metal bearing couples whose wear factor are an isotropic factor, Wang and his colleagues demonstrated that the wear factor of UHMWPE has a directional dependency due to multi-directional sliding [40-41]. This behavior is due to the fact that UHMWPE has long molecule chains compared to other polymers [41-42]. When UHMWPE slides against a metallic counter face, molecular chains preferentially become oriented along a so-called principal molecular orientation (PMO) resulting in a higher wear resistance of polyethylene. On the contrary, this phenomenon causes orientation softening in the perpendicular direction of the PMO, i.e. the cross-shear direction, leading to lowered wear resistance. This is the dominant reason for wear occurrence in metal-on-plastic (MoP) hip implants [15, 21, 41]. In addition to the anisotropy of wear in UHMWPE, the wear factor was observed to vary with the contact pressure [18, 20]. Kang et al. [21] formulated the wear factor with respect to the so-called cross-shear ratio based upon experimental data. Subsequently,

4

Kang and his colleagues proposed formulations to compute wear factor based on both cross-shear ratio and the contact pressure [22]. Making use of Kang et al experiments, Liu et al proposed a new wear formulation based upon the contact area with a dimensionless wear coefficient while not dependent on contact pressure as opposed to the Archard wear law [17].

Radiographs are commonly used to measure linear penetration of the femoral head inside the plastic cup, quantifying wear rates clinically [8]. From an engineering point-of-view, however, the variation in this measured surface profiles is not attributed just to wear, but also creep. As UHMWPE is a viscoelastic material, its deformation varies by time under loading, i.e. creep [43]. It was experimentally shown that 44% and 63% of total penetration in 32 and 22 (mm) acetabular cups were due to creep, respectively, after one million cycles [44]. Generally, it is not straightforward to distinguish wear from creep from in vivo penetration data. From a clinical perspective, it is of great interest to separate these elements, namely creep and wear, to gain a more realistic insight of true wear rates in vivo. Furthermore, creep varies with the load magnitude and direction, temperature, the load duration, and the geometry of bearing surfaces [43, 45].

Briefly, both contact pressure and sliding distance contribute to creep and wear of hip prostheses. Moreover, the wear factor is influenced by such parameters through the cross-shear ratio. The objective of the present study is thus to develop a fully integrated contact-coupled dynamic model based on multibody dynamics methodology to predict wear and creep in metal-on-polyethylene hip arthroplasties. This nonlinear dynamic model allows the

evaluation of both sliding distance and contact pressure, simultaneously, subjected to the walking condition. Such nonlinear multidisciplinary analyses are commonly expensive computationally. The current developed model is to reduce computational time significantly while a good accuracy is obtained. It is achievable as the method enables to determine contact stresses and forces during daily activities as a function of the penetration depth resulted from the dynamic analysis. On top of that, the damping property of the plastic cup is incorporated in the simulation, accounting for energy loss during contact and impact events. The wear rates in hip components are evaluated using Archard's wear law, whilst the cross-shear effect due to the polyethylene cup is taken into account. A creep model is also embedded in the developed model to evaluate creep penetration as a contributor to the damage in MoP hip implants. Parameters leading to creep and wear are interconnected and influenced by tribological properties of bearing surfaces, physiological loading and motions. Finally, the developed method is implemented to computationally study damage in polyethylene hip prostheses. For validation purposes, the acquired outcomes are compared to clinical data and numerical results reported in the literature. Separated linear creep and wear rates are also reported and corresponding maps were plotted, respectively. The effects of hip parameters, e.g. clearance size and hip radius on hip damage are also considered. Overall, the present study has innovatively developed a multibody dynamics model to evaluate both wear and creep while introducing a new closed-form contact model applicable to conformal soft hip prostheses, for the first time to the best of authors' knowledge. Moreover, the developed model

6

can significantly reduce the computational time required to simulate the dynamic motion of the hip implant and to compute wear and creep occurred on the bearing surfaces of MoP hip arthroplasties.

2. MATHEMATICAL MODELING

2.1. Dynamics of the hip implant

An artificial hip joint consists of two bearing surfaces, namely the femoral head and the acetabular cup. The femoral head is a spherical ball while the cup is of a hemisphere shape. Due to their different radii, the hip is a clearance joint with six degrees of freedom associated with its translational and rotational movements. Regarding the mechanism of total hip arthroplasty (THA), the femoral head is fixed to the femoral neck of a stem that is inserted in the intramedullary canal of the femur and the cup is embedded in the acetabular of the pelvis. In the human body, the femur and pelvis are attached to the rest of musculoskeletal system through joints, muscles and ligaments, among others. Thus, solving the dynamics of such a system is very complex. However, in vivo studies used instrumented hip implants to measure physiological motion and loadings at the center of the femoral head, which comprise the effects of all muscles, ligaments, ground forces, and so forth on the hip joint. Therefore, the unconventional cross section defined by Askari et al., which crosses the interface between the femoral head and femoral neck, is used to separate the femoral head from the femoral neck and stem [29, 46]. Consequently, that

7

complex dynamic system is reduced to a multibody system with two bodies, i.e. the femoral head and the cup. The cup embedded in the acetabular of the pelvis is also assumed stationary while the femoral head can freely move. Having access to such set of in vivo data, three-dimensional physiological loading is applied at the center of the head and the corresponding in vivo rotational motions are assigned to the femoral head owing to the fixed acetabular cup [29, 46]. Such a dynamic mechanism, including the femoral head and cup, is unconstrained and controlled by contact forces generated owing to the colliding bearing bodies [47]. A general representation of the head-cup articulation is depicted in Fig. 1. As the synovial capsule is preserved in THA, the artificial hip joint works under lubrication condition. However, the dynamic analysis developed in the present study neglects the existence of lubricant. This assumption will be discussed in the section 3.3.

The femoral head is called the body h that articulates against the hemisphere cup, the body c. P_h and P_c denote likely contact points located on the surfaces of the femoral head and cup, respectively. These points are located on the collision plane, which is a plane tangential to the surfaces of femoral head and cup at the contact point. The radial clearance size is defined as the difference between the radii of the bearing surfaces, $cl = R_c - R_h$, in which R_c and R_h are the cup and head radii. Moreover, the femoral head indents into the cup liner and the corresponding penetration size is δ as illustrated in Fig. 1. The centers of the femoral head and cup are denoted by O_h and O_c, respectively, and the vector that points from the point O_c to the point O_h is known as the eccentricity vector, **e**. The **n** and **t** also represent the unit vectors perpendicular and tangent

8

to the collision plane at the contact point. According to Fig. 1, K_c and K_h depict the mass centers of bodies c and h, respectively, to which body-fixed coordinate systems, $\xi_c \eta_c \zeta_c$ and $\xi_h \eta_h \zeta_h$ are attached, while XYZ designates the global coordinate system. The following expands a discussion on the kinematics of a hip joint. As illustrated in Fig. 1, the eccentricity vector, $\mathbf{e}$, is given by

$$\mathbf{e} = \mathbf{r}_h^O - \mathbf{r}_c^O \tag{1}$$

where both $\mathbf{r}_h^O$ and $\mathbf{r}_c^O$ are described as follows with respect to the global coordinate system,

$$\mathbf{r}_k^O = \mathbf{r}_k + \mathbf{A}_k \mathbf{S}_k^O \quad (k = c, h) \tag{2}$$

Moreover, the magnitude of the vector of the eccentricity is determined as

$$\begin{aligned} e &= \sqrt{\mathbf{e}^T \mathbf{e}} \\ &= \sqrt{\left(x_{O_c} - x_{O_h}\right)^2 + \left(y_{O_c} - y_{O_h}\right)^2 + \left(z_{O_c} - z_{O_h}\right)^2} \end{aligned} \tag{3}$$

The eccentricity unit vector is determined by $\mathbf{n}_e = \mathbf{e}/e$ and is normal to the collision surface [48-49], thereby aligning with the unit vector, $\mathbf{n}$, Fig. 1. Knowing the magnitude of the eccentricity vector, Eq. 3, and the clearance size, the so-called relative penetration can be computed by $\delta = e - cl$, which allows for detecting whether the cup and head are in contact. Moreover, the positions of

the contact points, P_h and P_c, onto the head and cup surfaces with respect to the global coordinate system, respectively, are expressed as

$$\mathbf{r}_k^P = \mathbf{r}_k + \mathbf{A}_k \mathbf{S}_k^O + R_k \mathbf{n}_e, \quad (k = c, h)$$

(4)

where R_k can be substituted by either the cup or head radius. Moreover, the velocities of the contact points are obtained by differentiating Eq. (4) with respect to time, yielding:

$$\dot{\mathbf{r}}_k^P = \dot{\mathbf{r}}_k + \dot{\mathbf{A}}_k \mathbf{S}_k^O + R_k \dot{\mathbf{n}}_e, \quad (k = c, h)$$

(5)

The time differentiation of the eccentricity unit vector, $\dot{\mathbf{n}}_e$, is computed according to its definition that is $\mathbf{n}_e = \mathbf{e}/e$. Finally, the relative velocity between the contact points (control points) is projected onto the normal and tangential directions, $\mathbf{n}$ and $\mathbf{t}$, denoted by $\mathbf{V}_N$ and $\mathbf{V}_T$ and given as:

$$\mathbf{V}_N = [(\dot{\mathbf{r}}_h^P - \dot{\mathbf{r}}_c^P)^T \mathbf{n}]\mathbf{n} = v_N \mathbf{n}$$

(6)

$$\mathbf{V}_T = (\dot{\mathbf{r}}_h^P - \dot{\mathbf{r}}_c^P)^T - \mathbf{V}_N \equiv v_T \mathbf{t}$$

(7)

2.2. Normal contact force model

It is known that modeling normal contact forces plays a crucial role in the dynamic behavior of mechanical systems. The contact force model must take into account not only material properties but geometric characteristics of the contacting bodies. From a numerical point-of-view, the contact constitutive law

10

should also be stable for the calculation of the contact forces allowing for the integration of the motion equations. As stated previously, a metallic femoral head and a polyethylene liner are contact pair elements in UHMWPE hip prostheses. The Young's modulus of the metal is about 210 GPa while the cup's is within the range of 0.1-2 GPa, which implies the metallic part can fairly be considered rigid in contact with the plastic component. Moreover, the resulting strains due to contact are not small compared to the size of engaged components any longer while compared to stiff hip bearings such as metal-on-metal implants. Another important characteristic of MoP hip prostheses is the conformity of the mating surfaces [49-50]. Therefore, physical characteristics of contact in MoP hip arthroplasties seriously violate assumptions made in the elastic half-space theory and it can be concluded that this theory is not applicable to the contact problem of such hip implants in particular. On the other hand, as the displacement at any point in the contact surface depends on the pressure throughout the whole contact, the solution of resultant integral equation based on the elastic contact theory for the pressure causes difficulties to obtain a closed-form contact equation. The main advantage of making use of a closed-form contact model in computational analyses is a considerable reduction of computational time and cost as it acts as a function of penetration depth that can be computed from the dynamic analysis as well as material and geometrical properties, thereby eliminating iterative solutions.

This difficulty is simplified in the elastic foundation model where the contact surface is modeled as a set of independent springs scattered over the contact surface [52]. Therefore, this model does not require computing deformations produced at all points on the bearing surface due to the pressure applied at one

11

point, thereby removing the integral nature of contact problems. This is contrary to what happens in elastic contact as the displacement at one location is influenced by the pressure applied at other locations. Nevertheless, the benefits of this simplification are (*i*) faster pressure calculations and (*ii*) facilitated analysis of conformal geometry, nonlinear materials, and layered contact. Readers interested are referred to the references Podra and Andersson [53] and Johnson [54]. In what follows, the elastic foundation is discussed in detail.

The springs spread onto the contact surface are considered as linear elastic bars with a stiffness of the contact. According to the laws of elasticity, the contact pressure for any spring in the elastic foundation for MoP hip implants in which only one of the bodies is assumed deformable is directly related to the spring deformation as [55-57]

$$P_i = K \frac{S_i}{\Gamma_i}, \ \ K = \frac{(1-\upsilon)E}{(1+\upsilon)(1-2\upsilon)} \tag{8}$$

where P_i is the contact pressure while E and υ stand for Young's modulus and Poisson's ratio of the elastic layer, respectively. Γ_i is the thickness of the elastic layer, which is referred as to the thickness of polyethylene liner. It is worth mentioning that comparing the stiffness of the polyethylene liner to the metallic backing, the metallic backing can fairly be assumed rigid. S_i also is the deformation of the spring, that is, the penetration depth along the normal direction to the undeformed contact surface. Kinetic analysis of the femoral head motion requires external forces to be calculated. Having the pressure

12

distribution function at hand, total normal contact force can be computed by integrating the resultant force due to the pressure at each element over the contact area, depicted in Fig. 2. To facilitate this process, the contact area and penetration depth are specified as functions of the contact angle, ψ. Assuming the femoral head penetrates the cup surface as can be seen in Fig. 2, the contact radius can be determined by intersecting two equations, Eq. (9a, b), of the cup and the femoral head in any two-dimensional cross section crossing the centers of hip components.

$$\text{The cup: } r_1 = R_c, \tag{9a, b}$$
$$\text{The femoral head: } r_2^2 - 2r_2 e \cos(\psi) + e^2 = R_h^2$$

where e is the size of the eccentricity vector and ψ is specified in Fig. 2. Moreover, r_1 and r_2 represent the radial distance of any point of the circles associated with the cup and femoral head, respectively, in the global coordinate system with respect to the origin at O_c, Fig. 2. (A) and (B) shown in Fig. 2 are points at which the circles defined by Eq. (9a, b) intersect. These can be determined by substituting r_2 with R_c, leading to the following expression

$$\psi_{max} = \arccos\left(\frac{R_c^2 - R_h^2 + e^2}{2R_c e}\right) \tag{10}$$

Solving the quadratic equation for r_2, (9b), the radial penetration of spring elements within the contact area can be calculated simply by the expression of $(r_2 - r_1)$, so

$$S(\psi) = (r_2 - r_1) \tag{11}$$

$$= e\cos(\psi) + R_h \sqrt{1 - \left(\frac{e}{R_h}\right)^2 \sin(\psi)^2}$$

$$- R_c$$

and the total normal contact force, f_n, can be determined by calculating the following integral:

$$f_n = \iint_\Xi P\mathrm{d}A \tag{12}$$

where Ξ is the contact area, $\mathrm{d}A$ can be written as $2\pi R_c^2 \sin(\psi)\cos(\psi)\mathrm{d}\psi$ and the pressure function as $\frac{K}{\Gamma} S(\psi, e)$ in which Γ is the liner thickness. The integration can, therefore, be performed over the interval $[0, \psi_{max}]$.

$$f_n = 2\pi \int_0^{\psi_{max}} \frac{K}{\Gamma} S(\psi) R_c^2 \sin(\psi)\cos(\psi)\mathrm{d}\psi \tag{13}$$

Substituting Eq. (11) into Eq. (13), it can be recast as follows:

$$f_n \tag{14}$$

$$= \int_0^{\psi_{max}} [e\sin(\psi)(\cos(\psi))^2 - R_c\sin(\psi)\cos(\psi)]\ \mathrm{d}\psi$$

$$+ \int_0^{\psi_{max}} \left[R_h\sin(\psi)\cos(\psi) \sqrt{1 - \left(\frac{e}{R_h}\right)^2 \sin(\psi)^2} \right]\ \mathrm{d}\psi$$

14

The first integration on the right side of Eq. (14) is straightforward to perform, but a new variable as '$\sin\varsigma = \left(\frac{e}{R_h}\right)^2 \sin(\psi)$' is defined to facilitate integrating the second term. After some mathematical manipulation, the total normal contact force can finally be expressed as

$$
f_n = \frac{2\pi K}{\Gamma} R_c^2 \left[\frac{e}{3}(1 - \cos(\psi_{max})^3) \right.
$$
$$
+ \frac{R_h}{3}\left(\frac{R_h}{e}\right)^2 \left\{ 1 - \left(1 - \left(\frac{e}{R_h}\right)^2 \sin(\psi_{max})^2\right)^{\frac{3}{2}} \right\} \tag{15}
$$
$$
\left. - \frac{R_c}{2}(1 - \cos(\psi_{max})^2) \right]
$$

However, this law is purely elastic in nature and cannot represent the energy loss during the impact process due to the viscoelastic property of polyethylene cup. The Kelvin-Voigt model can be used to simulate the viscoelastic behavior of polyethylene material. In the Kelvin-Voigt model, the energy loss was taken into account by a linear damping term [57]. The contact force model can therefore, be written in terms of a damping coefficient D as $f_n = H(\delta) + D\dot{\delta}$. Moreover, Hunt and Grossley suggested a hysteresis form for the damping coefficient as $D = \acute{\chi}H(\delta)$ [58]. Thus, the normal contact load can be given by [59],

$$
f_n \equiv f_n(\dot{\delta}, \delta) = H(\delta) + \acute{\chi}H(\delta)\dot{\delta} \tag{16}
$$

where $\dot{\delta}$ is the relative penetration velocity of the contact and $\acute{\chi}$ denotes the hysteresis damping factor for which a number of models are available in the

literature [59-61]. The hysteresis damping factor used in the present study is the viscous damping model proposed by Gonthier et al. and Zhang and Sharf as that also accounts for soft material contact with medium value of the coefficient of restitution [62-64], which leads to the final contact form given by

$$
\begin{aligned}
f_n = \frac{2\pi K}{\Gamma} R_c^2 \Bigg[& \frac{e}{3}(1 - \cos(\psi_{max})^3) \\
& + \frac{R_h}{3}\left(\frac{R_h}{e}\right)^2 \Bigg\{ 1 \\
& - \left(1 - \left(\frac{e}{R_h}\right)^2 \sin(\psi_{max})^2\right)^{\frac{3}{2}} \Bigg\} \\
& - \frac{R_c}{2}(1 - \cos(\psi_{max})^2) \Bigg] \\
& \times \left(1 + \frac{(1 - c_e{}^2)}{c_e}\frac{\dot{\delta}}{\dot{\delta}^{(-)}}\right)
\end{aligned}
$$

(17)

in which $\dot{\delta}^{(-)}$ denotes the initial impact velocity and c_e represents the coefficient of restitution [65-66]. In a vector form, the normal contact force applied to the femoral head can be written as

$$
\mathbf{F}_{p_h}^n = -f_n \mathbf{n}
$$

(18)

where f_n is a function of δ, i.e. the relative penetration depth. Additionally, the superscript *n* stands for the normal direction to the collision plane and the subscript P_h represents the contact point on the femoral head.

2.3. Dynamic governing equations of the system

In this sub-section, governing equations of system motion are given by employing the Newton-Euler equations of motion for unconstrained systems, as follows [27, 47, 67-68]:

$$\mathbf{M\ddot{q}} = \mathbf{g} \tag{19}$$

where **M** is the mass matrix of the hip joint, including both the moment of inertia and mass of articulating bodies, and **q̈** represents the acceleration vector. **g** also is a vector containing the gyroscopic and external forces acting on the femoral head from which the external forces are contact forces, physiological loading, and the moments acting on the femoral head. Contact forces are developed at potential contact points, P_c and P_h, when the bearing surfaces collide each other. The normal and tangential contact forces contributing to the force and moment vector, **g**, are effective provided that the system is in contact mode [67-69]. Assessing the following condition also helps detect time at which either impact or rebound takes place during the numerical solution by progressing time:

$$\delta\!\left(t^{i}\right) < 0, \quad \delta\!\left(t^{i+1}\right) > 0 \tag{20}$$

where δ is the penetration depth. Moreover, the rebound and impact velocities and location are to be acquired as initial conditions for solving the equations of

17

motion. Finally, the resulting equations are integrated using the adaptive Runge-Kutta-Fehlberg method over the time interval of interest [70]

2.4. Wear and creep simulation

Wear is the progressive loss of substance as a result of relative motion between surfaces. There are different wear mechanisms, e.g. abrasive, erosive, cavitation, adhesive, corrosive and oxidation, fatigue, fretting and minor wear mechanisms. Although some typical features of the wear process are demonstrated experimentally and there are some simple models to compute wear, such as the well-known Archard's wear methodology, no comprehensive laws of wear exist.

Two main mechanisms playing important roles in wear occurrence in polyethylene hip implants are the adhesive and abrasive. When two solids go to close contact, they adhere with another solid through their surface asperities. With the formation and rupture of asperity junctions built by the adhesion of asperities during sliding, either shearing along the interface or shearing within one of the asperities can take place. These cold welds between asperities can be broken due to shearing action, leading to material loss (wear). A simple model of wear was proposed by Archard [30] that was derived based on the assumption that two hard surfaces (i.e. cup and femoral head) contact each other through individual spots formed by the asperities across the contact surface of the mating bodies [71]. Another model used to predict wear is the Reye's hypothesis [72], which is an energy dissipative method correlating the volume of removed material to the work done by the tangential friction force.

In addition, the abrasive wear takes place once the polyethylene cup is loaded against wear debris, which is known as the third-body effect. Such particles can remove polymer material by micro-cutting and pull-out of individual grains, among others. A simple model to predict the abrasive wear presented in the reference [73] has an identical form to that of Archard's wear equation. These available models, e.g. Archard wear model, do not take into account microscopic effects such as asperity deformations and material tearing and so forth. These effects are considered through a macroscopic wear factor, which is measured experimentally. Archard's wear law is commonly adopted for its simplicity and validity in wide applications, even if it can describe only adhesive and abrasive wear mechanisms.

In addition to wear phenomenon, creep is the tendency of a material to deform permanently under the influence of mechanical stresses. The creep can occur in polyethylene cup, which is considered a viscoelastic material. The creep process can take place because of long-term exposure to high levels of stress that are still below the yield strength of the polyethylene. One of available models to consider viscoelastic behavior of the polyethylene material, providing information on the corresponding creep occurrence, is the Kelvin-Voigt model. Such a model represents the material by a Hookean spring and a Newtonian dashpot in parallel. Moreover, there are empirical formulations to determine creep behavior of the polyethylene materials such as the model developed by Lee and Pienkowski experimentally [43].

The correlation between creep and wear phenomena can be listed as follows: (1) in-vivo penetration measurement; and (2) the effect of viscoelastic material

19

on contact stresses. The Roentgen Stereophotogrammetric Analysis (RSA)

system is used to measure the linear and volumetric penetration of the femoral

head into the cup comparing three-dimensional geometric models of hip

components with stereo X-ray images [74-75]. However, measured penetration

is not just attributed to wear of polyethylene cup but also creep deformation.

Therefore, the in-vivo measurements cannot be useful to predict wear

magnitudes on hip implant surfaces, unless the penetration due to creep

deformation can be computed and discarded from the measurements.

From a mechanical point of view, the polyethylene cup also is a viscoelastic

material that can undergo creep, which affects the contact stresses as

$$\sigma = E\varepsilon + \eta \frac{d\varepsilon}{dt} \tag{21}$$

where σ is stress while ε stands for strain and E Young's modulus of the

polyethylene material. η also is viscous damping factor and $\frac{d\varepsilon}{dt}$ depicts the time

rate of strain. Therefore, such a contact stress influenced by the viscoelastic

property of polyethylene can affect wear computation and should be taken into

account.

2.4.1. Wear model

As the wear mechanism depends on contact pressure and sliding distance,

which vary by time and location, the cup-bearing surface is first divided into

finite size elements. Considering a spherical coordinate system with origin

located at the center of the acetabular cup, the bearing surface is discretized by

dividing the polar and azimuthal angles into differential size of π/ϱ radians, where ϱ is an integer. Figure 3 represents the cup surface discretized into finite elements, the contact area and those elements engaged in contact, schematically. Archard's wear model is commonly used in tribology to describe adhesive and abrasive wear mechanisms, although it is often adopted for a wide range of applications owing to its simplicity. Employing Archard's wear law, the linear wear rate can be computed using the following expression [30],

$$\frac{dh}{ds} = \frac{K_W P}{H} \tag{22}$$

in which h denotes the wear depth, while s stands for the sliding distance. K_W represents the dimensionless wear factor, P the contact stress and H finally is the hardness of the body engaged in contact with softer material. A forward numerical solution to predict linear wear rates, Eq. (22), can be acquired as follows:

$$h^{(k,j)}(t_{i+1}) = h^{(k,j)}(t_i) + k_W P^{(k,j)}(t_i) \Delta s^{(k,j)}(t_i) \tag{23}$$

where the term on the left side shows the total wear depth up to the $(i+1)^{\text{th}}$ time step at an element (k, j), while $h^{(k,j)}(t_i)$ is the corresponding wear term at the previous time step. The last term is the incremental wear depth, which is a function of the incremental sliding distance, the contact pressure and wear factor. The variable k_W is the wear factor ($k_W = K_W/H$), with unit $mm^3 N^{-1} m^{-1}$. According to Eq. (23), both contact pressure and incremental sliding distance

21

have to be computed before wear prediction at next time step. The sliding

distance and contact pressure are simultaneously acquired from the dynamic

analysis. The sliding distance vector is evaluated from the solution of Eq. (19),

and can be given at each time step by the following expression

$$\Delta\mathbf{s}(t_i) = \left(x^{P_c}(t_i) - x^{P_c}(t_{i-1})\right)\mathbf{i} + \left(y^{P_c}(t_i) - y^{P_c}(t_{i-1})\right)\mathbf{j} \\ + \left(z^{P_c}(t_i) - z^{P_c}(t_{i-1})\right)\mathbf{k} \tag{24}$$

and its magnitude, therefore, is

$$\Delta s(t_i) \\ = \sqrt{\left(x^{P_c}(t_i) - x^{P_c}(t_{i-1})\right)^2 + \left(y^{P_c}(t_i) - y^{P_c}(t_{i-1})\right)^2 + \left(z^{P_c}(t_i) - z^{P_c}(t_{i-1})\right)^2} \tag{25}$$

The increment of the sliding distance is estimated by Eq. (25) in which

$\left(x^{P_c}(t_i), y^{P_c}(t_i), z^{P_c}(t_i)\right)$ represents the location of the contact point on the cup

surface at the time (t_i). The element (k, j) positioning inside the contact area

undergoes a sliding distance of $\Delta s^{(k,j)}(t_i)$ which is equal to $\Delta s(t_i)$, calculated for

the contact point by Eq. (25) at the same time step. The pressure distribution is

also acquired from Eq. (8) and the corresponding contact radius can be

calculated from:

$$\frac{\overline{AB}}{2} = \sqrt{R_c^2 - \left(\frac{R_c^2 - R_h^2 + e^2}{2e}\right)^2} \tag{26}$$

22

The angle ψ illustrated in Fig. 2 is defined between the vectors, $\overrightarrow{O_cQ}$ and $\overrightarrow{O_cP_c}$ where Q is an arbitrary point located onto the cup surface. The scalar product of those vectors yields Eq. (27) by which ψ can be determined.

$$\overrightarrow{O_cP_c} \cdot \overrightarrow{O_cQ} = R_c^2\cos(\psi) \tag{27}$$

We assume that the angle ψ belongs to an element (k, j) on the cup surface and is shown as $\psi^{(k,j)}$. An element with an angle $\psi^{(k,j)}$, calculated from Eq. (27), greater than ψ_{max} locates outside of the contact area at that specific time step and its corresponding pressure is zero. Otherwise, the pressure, $P^{(k,j)}(t_i)$, is computed from the following equation which is extracted from Eq. (8) and is a function of $\psi^{(k,j)}$.

$$P\big(\psi^{(k,j)}\big) = \frac{(1-v)}{(1+v)(1-2v)}\frac{E}{\Gamma}\Bigg[e\cos(\psi^{(k,j)}) + R_h\sqrt{1-\left(\frac{e}{R_h}\right)^2\sin(\psi^{(k,j)})^2} - R_c\Bigg] \tag{28}$$

Due to sliding hip components against each other, the area swept through the sliding at a time step has to be computed. Obviously, the contact area covers a number of surface elements having positive contact pressures, as shown in Fig. 3. The linear wear rate in each element (k, j) within the contact area varies in connection with the Archard's wear law [27, 76]. In each integration time step of the dynamic simulation, the linear wear depth computed for each element of the bearing surface is stored in a corresponding cell of an array. Eventually at

23

the end of the numerical simulation, accumulated wear at each element is computed by the summation of all partial linear wear rates stored during a gait cycle. The overall magnitude of wear can consequently be given by [27, 72]

$$h_{total}^{(k,j)} = \sum_{i=1}^{n} h^{(k,j)}(t_i)$$

(29)

where (*k*, *j*) specifies an element of the cup surface and *n* is total number of time steps through which the numerical wear simulation is performed.

2.4.1.1. Cross shear ratio

The cross shear ratio can be quantified as the ratio of the frictional work along the cross-shear direction to the total frictional work over a cycle of any daily-activity [15, 21, 41]. In order for the determination of this quantity, one needs to identify the so-called principal molecular orientation (PMO). It is assumed that polymeric chains preferentially align with the direction of the dominant frictional work regarding the physical definition obtained based upon experiments [6, 41-42]. The PMO can therefore be determined as the direction that minimizes the cross-shear ratio. The cross-shear ratio ($\Im$) is defined as the frictional work computed for the set of friction force and displacement vectors perpendicular to the PMO direction ($W_{\text{cross-shear}}^{f}$), divided by the total frictional work (W_{total}^{f}), [16, 19, 23, 77], as given by.

24

$$\Im = \frac{W_{\text{cross-shear}}^{f}}{W_{\text{total}}^{f}} \tag{30}$$

The friction work can be calculated based on $W^f = \sum_{i=1}^{n} \mu f_n(t_i) \Delta s(t_i)$ where μ is friction coefficient, f_n denotes normal contact force and $\Delta s(t_i)$ the incremental sliding distance. Regarding the vector of the incremental sliding distance, $\Delta \mathbf{s}(t_i)$ given by Eq. (24), the direction (φ_f) of incremental motion along the contact point trajectory can be calculated. Moreover, considering a test PMO direction (axis), from a set of blue arrows shown in Fig. 4, originated from the center of the acetabular cup with an angle φ, frictional force and incremental sliding distance components parallel to and perpendicular to that axis can be calculated for each increment [15-16, 19]. Assuming that the friction coefficient does not vary during a cycle, the cross shear can be formulated as follows:

$$\Im = \frac{\sum_{i=1}^{n} f_n(t_i)\left(\sin\left(\varphi_f(t_i) - \varphi\right)\right)^2 \Delta s(t_i)}{\sum f_n(t_i) \Delta s(t_i)} \tag{31}$$

The dynamic model developed in the previous sections obtains the sliding distance and contact force with time, which allows calculating Eq. (31) for each angle φ, from 0 to π, until the principal molecular orientation, φ_{PMC}, is reached where the cross-shear ratio is minimized. Analyzing experimental results, Kang et al expressed the wear factor as a function of the cross-shear ratio as follows [21].

$$k_w = 3.28 \times 10^{-7} \ln(\Im) + 1.62 \\ \times 10^{-6} \ \text{mm}^3\text{N}^{-1}\text{m}^{-1} \tag{32}$$

This wear factor model depends on just the cross-shear and not contact pressure, Eq. (32). The volumetric wear rate is numerically evaluated as a function of contact force, sliding distance and wear factor. As the contact force is the same for all scenarios considered and the sliding distance does not vary significantly when clearance size changes, the predicted volumetric wear rates, thus, do not show a recognizable variation with such hip parameters. This is a limitation of that model as it has experimentally been illustrated the wear factor is dependent on the contact pressure as well. When the contact pressure increases, e.g. with increasing the clearance size, the wear factor decreases as can be deduced from Eq. (33). Therefore, the modified wear factor model presented by Kang et al. can provide outcomes that are more realistic [22].

$$k_w(\Im, \bar{p}) = \exp[-13.1 + 0.19\ln(\Im) \\ - 0.29\bar{p}] \tag{33}$$

where $\bar{p}$ is the average contact pressure for a given element, which is determined by averaging contact stress over one gait cycle.

2.4.2. Creep model

UHMWPE is a viscoelastic material, that is, deformation varies by time under loading (creep). Therefore, surface changes reported clinically are not just

associated with wear but also creep. Lee and Pienkowski [43] performed

uniaxial creep tests to identify the creep characteristics of orthopedic grade

extruded UHMWPE compressed with constant pressures of 2, 4 and 8 MPa

under the physiologic condition for 10,000 min. Their findings can be

summarized in the following equation, which shows the creep penetration

depends on both pressure and a logarithmic timescale [79]:

$$
\delta_{Creep}^{(k,j)} = \left[3.491 \times 10^{-3} + 7.996 \right.
$$
$$
\times 10^{-4} \left(log \left(N \sum_{i=1}^{n} \Delta^{(k,j)} t_c(i) \right) \right.
$$
$$
\left. \left. - 4 \right) \right] \frac{\sum_{i=1}^{n} P^{(k,j)}(t_i) \Delta^{(k,j)} t_c(i)}{\sum_{i=1}^{n} \Delta^{(k,j)} t_c(i)} \Gamma^{(k,j)}
$$

(34)

where $\delta_{Creep}^{(k,j)}$ is the linear damage at an element (k, j) due to creep, N is the

total number of cycles in service. $\Gamma^{(k,j)}$ is the thickness of element (k, j) of the

acetabular cup and $\Delta^{(k,j)} t_c(i)$ associated with an element (k, j) of the cup

surface is non-zero just when the corresponding i is in the set of time values

where the contact stress is non-zero. The unit of time and pressure are minute

and MPa, respectively, according to Lee and Pienkowski experiment. It should

be noted that this model does not incorporate creep recovery so zero

relaxation is assumed. According to the discretized cup surface, elements

involved in the contact area are identified for which the time step and the

contact pressure multiplied by the time step are calculated and stored. At the

end of the simulation, the corresponding accumulated terms of Eq. (34) are

available to compute damage associated with the creep at each element on the cup surface.

2.5. Numerical solution procedure

The equations of motion are formulated as is presented in Eq. (19). The term on the right-hand side of this equation depicts the force vector, which can be written as

$$\mathbf{g} = \mathbf{F}_b + \mathbf{F}_{p_h}^n + \mathbf{F}_f \tag{35}$$

where $\mathbf{F}_b$ is the body force of the femoral head while $\mathbf{F}_{p_h}^n$ is the normal contact force presented in Eq. (18). Moreover, $\mathbf{F}_f$ represents the three-dimensional physiological loadings, due to muscles and ligaments, ground-reaction force and so on, measured in vivo. Three-dimensional physiological forces obtained in vivo by Bergmann et al using instrumented hip implants are plotted in Fig. 5 [80]. In addition to the physiological loadings, the in vivo angular motions, presented in Fig. 6 [80], are assigned to the rotational motion of the femoral head as was previously stated in the section 2.1.

The equations of motion, Eq. (19), should be integrated over time to determine the dynamic response of the system before computing wear and creep. The adaptive Runge-Kutta-Fehlberg method, RK45, is employed to do this time integration. To acquire accurate and stable outcomes, an error threshold is defined. At each time step of dynamic simulation, the error magnitude is

assessed by comparing results obtained from the explicit method with different orders. When the error magnitude is greater than the error threshold, the time step is halved and computation re-done. In this process, the minimum value for the integration step size is considered to be 1e-5 s and the corresponding integration tolerance 1e-6.

Knowing the dynamic behavior of the hip implant, the principal molecular orientation is determined employing the method explained in the section 2.4.1.1. The cross-shear ratio is then computed using Eq. (31), which allows the calculation of the wear factor, Eq. (32). According to the model developed, the cup surface is discretized into several finite elements. The accuracy and convergence study are also performed to evaluate the mesh density. To achieve that, the azimuthal and polar angles of the spherical coordinate systems at the center of the cup are differential angles with the size π/ϱ, where ϱ is an integer. Consequently, the elements are not uniform and the accuracy of the results and convergence of the method are assessed with increasing ϱ that means the increase of the mesh density.

At each time step, t_i, the location of the contact point is known from the dynamic solution. ψ_{max} is determined from Eq. (10) and contact pressure at each element, (k, j), is computed based on the procedure explained in the section 2.4.1, Eqs. (27) and (28). Moreover, the sliding distance is evaluated using Eq. (25). The wear increment at the integration time step, t_i, and the element (k, j) is computed according to the second term on the right side of Eq. (23). This wear increment is stored and at the end of the wear simulation, the amount of wear accumulated on an element is the sum of all partial wear

magnitudes obtained over numerical simulation at that specific element. The present study does not consider the surface evolution due to the wear and creep. Therefore, the wear of the running in phase (up to one million cycles) is obtained by multiplying wear magnitude evaluated after one gait cycle by N that is the number of simulation cycles.

In order to compute the creep deformation, contact pressure at an element (k, j) at each time step, t_i, is determined according to Eqs. (27) and (28) while knowing ψ_{max}. Pressure amount is multiplied with the size of time step and stored until the end of simulation, the summation of $\sum_{i=1}^{n} P^{(k,j)}(t_i) \Delta^{(k,j)} t_c(i)$ in the Eq. (34) is computed. If pressure value at the element (k, j) is not zero, the size of time step is included in the summation $\sum_{i=1}^{n} \Delta^{(k,j)} t_c(i)$, Eq. (34). Knowing these two parameters, the average pressure and logarithmic time are computed, which allows determining the creep deformation of polyethylene hip implant after one million cycles in service. It would be mentioned that the present study assumed that the geometry updating of the polyethylene liner does not affect the contact stresses and the trajectory of the femoral head in the running in phase (up to one million cycles). Therefore, these two terms, $\sum_{i=1}^{n} P^{(k,j)}(t_i) \Delta^{(k,j)} t_c(i)$ and $\sum_{i=1}^{n} \Delta^{(k,j)} t_c(i)$ remain unchanged for all walking cycles, which means they need to be computed just for one walking cycle.

2.6. Example analysis

As a demonstrative example of application, a standard hip prosthesis with the acetabular cup of 28 mm diameter, a clearance size of 80 μm and a liner thickness of 8 mm is studied. The femoral head is made of Co-Cr-Mo metal alloy with a Young's modulus 210 GPa, Poisson ratio and density of 0.3, and 8330

kg/m^3, respectively, while the UHMWPE acetabular cup has a Young's modulus 0.5 GPa, Poisson's ratio 0.4 and a restitution coefficient 0.7. The wear factor for MoP couple is calculated from Eq. (32), unless otherwise stated. In the present study, the minimum value for the integration step size to solve the equations of motion is considered to be 1e-5 s while wear is computed at each 70 time steps, that is, 7e-4 s is the step size of wear computation. Moreover, the cup surface is discretized into several elements and a value of the parameter ϱ equal to 360 guarantees the accuracy and convergence of the solution. Implementing the method explained in the section 2.4.1.1. to determine the principal molecular orientation results in the cross-shear ratio with respect to the angle of test axis, φ, depicted in Fig. 7. The minimum $\Im$ occurs at the intersection of the red line with the curve as shown in Fig. 4 and φ_{max} is found to be 107˚. Its orientation is also illustrated in Fig. 4 by red dashed line. Comparing the outcomes with those available in the literature allows for the validation of the developed approach. The same standard hip implant as the example defined above is used while two sizes of hip implants, 28 and 22 mm are considered to predict wear in polyethylene hip implants. The acquired outcomes are compared to those from clinical studies and numerical investigations. Moreover, a comparison of total damage, consisting from linear wear and creep, is carried out with those reported by clinical studies, using the same standard hip implant characterized as the demonstrative example. From an engineering point of view, it is worth considering effects of design parameters on wear and creep in hip athroplasties as these outcomes can result in optimal designs of hip implants undergoing lower damages in service,

which can increase their lifetime. Therefore, effects of hip prosthesis size and clearance size on linear and volumetric wear rates and linear creep are considered. In this regard, four different hip implant sizes, namely 22, 28, 32 and 36 mm, are considered to investigate the influence of hip implant size on wear and creep. Moreover, multiple sizes of clearance (20, 40, 80, 100 and 200 μm) are investigated to find out how creep and wear values are influenced by the clearance size. It is worth mentioning that the same standard hip implant characterized above is used to investigate the influence of design parameters on wear and creep amounts.

Regarding Lee and Pienkowski creep model obtained experimentally [43], the creep strain increases linearly with logarithmic time (minutes) and pressure (MPa). The present study acquires these two leading terms. Lee and Pienkowski reported that creep strains associated with pressure magnitudes of 4 and 8 MPa magnitude are 0.012 and 0.026, respectively, after 10000 minutes of test. A logarithmic time difference of maximum in-service duration of a hip implant after one year and the maximum test duration of the experiment is about 6.25%. Therefore, it is possible to obtain creep based on the plots reported by Lee and Pienkowski from their experiment. This analysis is carried out and elaborated in the result section.

3. RESULTS AND DISCUSSION

The computational time efficiency of the developed model is the first to be commented in this section. The total computational time consumed to solve

the motion equations and to acquire wear and creep values for the present method was no longer than 25 minutes (on a 2.7 GHz personal computer with Intel® Core(TM) i7-6820HQ CPU). However, Gao et al. reported a total computational time for just solving motion equations of about 4 and 5 hours for implicit and explicit finite element simulations, respectively, on a 3.5 GHz personal computer [81]. Therefore, the developed model can be used to perform parametric studies for optimizing and assessing new implant designs due to relatively low computational time. Moreover, one of main goals to decrease computational time is to create independent software tools to help doctors make an optimal decision for patient-specific implants as fast and accurate as possible. Such a decision can be made taking into account patient factors and parameters such as physiological loadings/motions associated with different daily activities, activity level, age, gender and so forth. Considering a FE code that can be run independently without any support of a commercial software to reduce costs involved, the FE modeling would still be a time consuming option in order to consider multiple loadings and motion scenarios.

3.1. MoP hip damage: creep and wear

The contour of average pressure distribution and logarithmic time $(log(N\sum_{i=1}^{n}\Delta^{(k,j)}t_c(i))$, Eq. (34)) contributing to the creep according to Lee and Pienkowski creep model is presented in Fig. 8. From the results obtained, the maximum average pressure of an element, (k, j), on the cup surface is 5.4 MPa. The creep strain allocated to this number after 10000 minutes of test according to Lee and Pienkowski experiment is 0.018. For a cup of 8 mm thickness, the

creep penetration results in 0.144 and after modification by adjusting the difference of service duration according to Lee and Pienkowski experiment the result becomes 0.153, conforming with our obtained result which is 0.158. The contact point trajectory is also illustrated in Fig. 8 by projecting it onto the plane inclined from the horizontal plane with an angle of 45 degrees. The creep distribution onto the cup surface aligns with the contact point path and the zone where maximum creep penetrations occur can be considered inside the trajectory line. As can be observed in the figure, the creep distribution does not have a regular shape. Although a circular zone with highest creep values is seen, an extension with red color exists on its top, which leads to irregularity. The same pattern can be found for the average pressure distribution (Fig. 8). In order to get an idea of what can lead to this irregularity, one needs to look in the contributing parameters, e.g. pressure and time period during which an element is under pressure. Two instants of the walking cycle, points (A) and (B), are illustrated in Fig. 8, which correspond to 0.1 and 0.55 s of the gait, respectively. The value of maximum contact stress does not go below 7.5 MPa during the time the contact point moves from the point (A) to (B). Moreover, the walking cycle according to in vivo data used in the present study lasts 1.1013 s. The sliding distance from the beginning of the gait to the time the contact point coincides with the point (B) forms 37.5% of the whole sliding distance over a walking cycle. In addition, the time taken until the contact point reaches the point (B) is about half of the gait duration. It can imply that the left and top-left sides of the slide track undergo high contact stresses for a relatively long time, which can be considered the main cause of the irregularity

observed in the creep map. It is worth noting that high contact stresses undergone by the hip, Fig. 9a, are associated with the stance phase and the single support of the walking gait cycle.

Figure 9 represents wear map onto the cup surface as well as leading factors, namely contact pressure and sliding distance. As is observable, the wear distribution complies with the contact point path onto the cup. The maximum linear wear rates also occur within the area illustrated by the dark red color in the wear contour. Moreover, the maximum sliding distance calculated by this model is 23.5 mm, conforming to the references [81-82]. The contact radius ranges from 8 to 11.6 mm and highest wear rates occur inside or in proximity of the contact path line. Moreover, Table (1) and (2) present wear results for hip implants with sizes 28 and 22 mm, respectively. These tables also enable us to compare those results with clinical data and results acquired by other numerical methods. A good agreement can be seen among results. It is worth stating that Eq. (23) is written using the Euler integration algorithm which is a simplistic integration scheme. Hence, the two-step and three-step Adams-Bashforth method are also employed to assess how accurate the Euler integration algorithm is for the wear model developed in the current study. Acquired outcomes show that the integration scheme employed in the current study is promising for the present numerical set-up.

Retrieval analyses show higher wear rates in MoP hip prostheses while compared to numerical studies. It occurs as hip prostheses are considered well-positioned in computational analyses while it is not the case in reality particularly with the occurrence of micro-separation, edge-loading and hip

component malposition. Totally, it is very difficult to do a comparison with clinical data as wear in vivo depends on many factors such as age, body weight, activity level and PE oxidation, among others. Although results acquired by computational methods align with the developed model, discrepancies are observable due to differences in the loading and motion inputs and hip sizes, e.g. liner thickness and clearance size, among others. It is worth noting that, in Table (1), the size of hip implant and the liner thickness used by the present study and the references [82, 84] are identical, which are 28 mm and 8 mm, respectively. Moreover, the hip implant size and liner thickness used by the present study and the references [82, 84] are 22 mm and 8 mm, respectively, to acquire results presented in Table 2. However, the above references did not report the clearance size. Moreover, the liner thickness and clearance size were not reported in the reference [88]. Other references listed in Tables (1), (2) and (3) are clinical studies, which have studied a group of polyethylene hip implants that have different sizes.

It is worth noting that the loading and motion inputs influence wear in hip prostheses. Fialho et al. [89] observed a two-fold increase in the wear rates taking place during a modelled jogging cycle in comparison with those of the walking cycle, owing to a considerable increase in loading. The motion inputs, i.e. the rotational motions between the femoral head and cup, influence both the sliding distance and the cross-shear ratio contributing to wear magnitudes and distribution. Liu et al. reported that the evaluated volumetric wear values of a hip implant working under the motion inputs from the ProSim simulator and the ISO motion for the walking cycle were 13% and 4% less, respectively,

than that predicted from in-vivo walking motion [90]. Moreover, one study obtained that using a 3D sliding distance increased volumetric wear by 18% compared to a simplified two dimensional flexion-extension analysis [89]. Therefore, a future-research direction in this field is to study how any daily activity contributes to wear in hip arthroplasties as well as to evaluate the corresponding contact-point trajectory generated onto the bearing surfaces. Contours of linear wear, creep and overall damage, which consist of both wear and creep, are also illustrated separately in the plot (Fig. 10). The results show that creep accounts for a significant proportion of surface penetration on PE cup bearings, corroborating with both experimental and clinical studies [44, 91-93]. Moreover, the present study focuses on the first year behavior of wear and creep in hip implants, and evaluates total linear penetration (total damage) of the femoral head into the polyethylene cup, as can be seen in Fig. 10. The reason behind of just considering the first million cycles is that creep becomes relatively constant while wear steadily increases after this duration [44, 91]. Understanding the first year performance of hip implant, therefore, reveals very important information from technical and biomedical points of view and enables to estimate wear and creep in following years. Hip damage that is the combined wear and creep, also referred to as the penetration depth, is presented in Table 3, while compared to clinical measurements. This comparison shows a good agreement among outcomes. This set of results is useful and helpful to better understand the interaction of creep and wear in THA and to estimate true wear rates and creep from in vivo measured penetration data. It is worth mentioning that the present study does not take

37

into account updating the geometry of bearing surfaces due to material loss during numerical analysis, which may affect the creep and wear results.

3.2. The size of hip implant and clearance

The influences of hip size and clearance size on predicted wear and creep are considered in Tables 4 and 5. It can be seen in Table 4 that an increase in hip implant size increases the volumetric wear of the liner since it leads to widening the contact point trajectory and subsequently affecting the sliding distance on which the wear depends. However, the hip implant size causes linear wear and creep to decrease as the clearance size remains fixed and an increase in hip size decreases the contact pressure influencing not only creep, but wear. In contrast, linear wear and creep increase with clearance size, while it does not affect the volumetric wear as can be seen from Table 5. The higher radii difference, the greater contact pressure, thereby rising wear and creep in MoP hip implants. Clearance size slightly changes volumetric wear rates, which can be neglected. However, using the modified wear factor, Eq. (33), enables us to take into account the influence of pressure variation on wear factor, which addresses the variation of volumetric wear due to a change in the clearance size. Using Eq. (33) to compute the wear factor at each element engaged in contact, the effect of clearance size on the volumetric wear rate is re-considered. As can be seen in Table 5, the volumetric wear rate decreases with increasing the clearance size. A question raised here is why are volumetric wear rates predicted by Eq. (33) less than those from Eq. (32)? The answer can be found in the wear factor values obtained by such two models. The wear factor

calculated from Eq. (32) does not vary with contact pressure and is constant for all elements, i.e. about 1.15e-6 $mm^3N^{-1}m^{-1}$. However, the wear factor obtained using Eq. (33) at an element in contact area with an average pressure of 2 MPa is 0.87e-6 $mm^3N^{-1}m^{-1}$, approximately. Therefore, the magnitude of wear factor for much of elements engaged in contact is less than that acquired by Eq. (32), leading to less volumetric wear rates. However, it is worth mentioning that the average pressure for those elements outside of the contact area is zero and their corresponding wear factor computed by Eq. (33) is 1.56e-6 $mm^3N^{-1}m^{-1}$. Wear and creep behaviors with respect to changes in hip geometric parameters discussed above align with the references [5, 8].

In contrary to a decreasing trend seen in linear wear rates acquired by Eq. (32) with increasing hip size, an upward trend is observed once Eq. (33) is employed for wear prediction. The later trend is in agreement with that reported by Kang et al [22] while the one from Eq. (32) aligns with the reference [8]. Using the wear factor computed by Eq. (32), a considerable increase (123%) in linear wear rates is observed comparing the outcomes for the hip with clearance sizes of 20 and 200 μm. On the other hand, the wear model employing the wear factor that is dependent upon both contact pressure and cross-shear ratio does not show a notable sensitivity to the change of clearance size (less than 10% increase). Such trends resulted from using available models to compute the wear factor are controversial. Therefore, performing experimental tests to investigate the effects of hip parameters, e.g. hip size and clearance size, on linear wear values in order to assess which model can provide more realistic results is inevitable.

3.3. Model limitations and future research directions

The present study assumed that the geometry evolution of the polyethylene cup owing to material loss and creep deformation does not affect the contact stresses whereby the wear magnitude varies linearly during the wear analysis that is limited to the running in phase (up to one million cycle). Surface evolution leads to a reduction in contact stresses over time, resulting in decreasing wear rates and creep deformation. Therefore, it can be deduced that the present study overestimated linear wear rates and creep deformation that are dependent on contact pressure. In order to extend the presented method to update bearing surfaces, Eq. (8) should be used while determining contact stresses iteratively. Unfortunately, the pressure function, Eq. (28), cannot be used considering surface variations of plastic surface due to wear and creep phenomenon as that function was derived based on the contact of a sphere object with a hemisphere body. The ongoing research aims to extend the model to take the geometry evolution owing to wear process into account. The improved model will address the effect of the geometry update on both contact stresses and contact point trajectory (sliding distance).

It also is worth noting that the presented model is unable to address accurate contact pressure and contact area once the edge-loading occurs due to the simplification of the model that limits it to capture the geometry change at the cup edge. This issue raises with using the Hertz contact model as well. The FE method, therefore, should be employed to analyze the edge-loading

phenomenon. However, one of future research directions can be to develop a simplified continuum elastic model to capture edge-loading.

Moreover, the synovial capsule is preserved in total hip arthroplasties (THA) and the hip implant works under lubrication condition. However, the present study neglected the lubrication presence in the numerical analysis. It is worth mentioning that the wear factor formulation, Eqs. (32) and (33) were obtained from experimental tests where the effect of lubricant was also taken into account. Therefore, the developed model accounts for lubricant effect to some extent. However, it has been indicated that the wear varies with the film thickness over a normal walking cycle [97], which cannot be addressed by the present model taking a fixed magnitude of wear factor during numerical analyses. Moreover, the existence of lubricant can cause the trajectory to deviate from that in a dry hip implant. The interaction between the lubricant and structure as well as the contact of surface asperities can also lead to vibrating the femoral head inside the cup with micrometer and nanometer of amplitudes due to either fluid-induced vibration or friction-induced vibration [29, 98]. These two can result in a change in the contact point trajectory at both micro and macroscales, which can affect the final wear and creep profiles. In order for obtaining more realistic wear results, the existence of lubricant should be taken into account both in dynamic and wear/creep models as is the future direction of this on-going research.

Finally, the model as is presented in the present study requires physiological loadings and motion as input, which limits its use for patient specific studies. Therefore, adding the developed model as a subroutine to a musculoskeletal

modeling software can enable the model to be used in performing patient-specific studies considering the effect of different daily activities, gender, BMI and activity level, among others on tribology performance of hip prostheses.

4. CONCLUSION

A nonlinear dynamic model was developed to study polyethylene damage in MoP hip implants, resulted from compressive creep and wear. Totally, this study presented specific characteristics as (1) a fully integrated contact-dynamic model; (2) a closed-form contact formulation; (3) an analysis of both sliding distance and contact mechanics simultaneously; (4) a study of not only wear, but also creep as contributors to UHMWPE hip damage. The model was verified against clinical studies and those employing numerical methods. From the analysis performed, it can be concluded that linear wear and creep magnitudes increase with clearance size, while hip size showed inverse effects on such parameters. Moreover, it was illustrated that volumetric wear decreases with increasing the clearance size. These results are helpful and useful for either modifying available hip designs or designing new hip implants as well as for technical-based decision criteria for clinicians. The creep mechanism was explained using outcomes acquired for leading parameters, time and pressure, regarding Lee and Pienkowski experimental model. The contributing role of sliding distance, contact pressure and contact area on the wear were analysed physically. It was illustrated that the creep and wear distribution onto the cup surface conformed to the contact point path and the

42

zones where maximum creep and wear occurred were inside the trajectory

line. Although the wear distribution had a regular shape, the creep distribution

showed an irregularity. Finally, the model can be used for parametric studies as

it is very fast, less than 25 minutes computational time, with a good accuracy.

ACKNOWLEDGMENT

REFERENCES

[1] Kurtz S., Ong K., Lau E., Mowat F., Halpern M., Projections of primary and revision hip and knee arthroplasty in the United States from 2005 to 2030. The Journal of Bone & Joint Surgery, 89(4) 780-785 (2007)

[2] Canadian Joint Replacement Registry 2014 Annual Report. Canadian institute for health information. Canada2014.

[3] NJR 10th Annual Report 2013, National Joint Registry UK 2013.

[4] Askari E., Flores P., Dabirrahmani D., Appleyard R., A review of squeaking in ceramic total hip prostheses. Tribology International 93 239–256 (2016)

[5] Liu F., Fisher J., Jin Z., Computational modelling of polyethylene wear and creep in total hip joint replacements: Effect of the bearing clearance and diameter. Proc IMechE Part J: J Engineering Tribology 226(6) 552–563 (2012)

[6] Turell M., Wang A., Bellare A., Quantification of the effect of cross-path motion on the wear rate of ultra-high molecular weight polyethylene. Wear 255(7–12) 1034-1039 (2003)

[7] Clarke, I.C., Good, V., Williams, P., Schroeder, D., Anissian, L., Stark, A., Oonishi, H., Schuldies, J., Gustafson, G., Ultra-Low Wear Rates for Rigid-on-Rigid Bearings in Total Hip Replacements. Proceedings of the Institution of Mechanical Engineers, Part H: Journal of Engineering in Medicine, 214(4) 331-347 (2000)

[8] Bevill S.L., Bevill G.R., Penmetsa J.R., et al. Finite element simulation of early creep and wear in total hip arthroplasty. J Biomech 38 2365–2374 (2005)

[9] Dumbleton J.H., Manley M.T., Edidin A.A., A review of the manuscript between wear rate and osteolysis in total hip arthroplasty. Journal of Arthroplasty 17 649–661 (2002)

[10] Affatato S., Taddei P., Carmignato S., Modena E., Toni A., Severe damage of alumina-on-alumina hip implants: Wear assessments at a microscopic level. Journal of the European Ceramic Society, 32(14) (2012) 3647-3657

[11] Nevelos J.E., Ingham E., Doyle C., Nevelos A.B., Fisher J., Wear of HIPed and non-HIPed alumina-alumina hip joints under standard and severe simulator testing conditions. Biomaterials, 22, 2191-2197 (2001)

[12] Dowson D., Jin Z., Metal-on-metal hip joint tribology. Proceedings Institution of Mechanical Engineers Part H: Journal of Engineering in Medicine, 220, 107-118 (2006)

[13] Maxian T.A., Brown T.D., Pedersen D.R., Callaghan J.J., A sliding-distance-coupled finite element formulation for polyethylene wear in total hip arthroplasty. Journal of Biomechanics 29(5) 687-92 (1996)

[14] Raimondi M.T., Santambrogio C., Pietrabissa R., Raffelini F., Molfetta L., Improved mathematical model of the wear of the cup articular surface in hip joint prostheses and comparison with retrieved components. Proceedings of the Institution of Mechanical Engineers; Part H; Journal of Engineering in Medicine 215(4) 377–391 (2001)

[15] Kang L., Galvin A.L., Brown T.D., et al. Quantification of the effect of cross-shear on the wear of conventional and highly cross-linked UHMWPE. J Biomech 41(2) 340-346 (2008)

[16] Goreham-Voss C.M., Hyde P.J., Hall R.M., et al. Cross shear implementation in sliding-distance-coupled finite element analysis of wear in metal-on-polyethylene total joint arthroplasty: intervertebral total disc replacement as an illustrative application. J Biomech 43(9) 1674-1681 (2010)

[17] Liu F., Galvin A., Jin Z., Fisher J., A new formulation for the prediction of polyethylene wear in artificial hip joints. Proceedings of the Institution of Mechanical Engineers, Part H: Journal of Engineering in Medicine 225(1) 16-24 (2011)

[18] Wang A., Essner A., Klein R., Effect of contact stress on friction and wear of ultra-high molecular weight polyethylene in total hip replacement. Proceedings of the Institution of Mechanical Engineers, Part H (Journal of Engineering in Medicine) 215(H2) 133-139 (2001)

[19] Mattei L., Di Puccio F., Ciulli E., A comparative study of wear laws for soft-on-hard hip implants using a mathematical wear model. Tribol. Int. 63, 66-77 (2013)

[20] Barbour P.S.M., Barton D.C., Fisher J. ,The influence of stress conditions on the wear of UHMWPE for total joint replacements. J Mater Sci Mater Med 8(10) 603–611 (1997)

[21] Kang L., Galvin A.L., Brown T.D., Fisher J., Jin Z., Wear simulation of ultra-high molecular weight polyethylene hip implants by incorporating the effects of cross-shear and contact pressure. Proceedings of the Institution of Mechanical Engineers, Part H (Journal of Engineering in Medicine) 222(H7) 1049–1064 (2008)

[22] Kang L., Galvin A.L., Fisher J., Jin Z., Enhanced computational prediction of polyethylene wear in hip joints by incorporating cross-shear and contact pressure in additional to load and sliding distance: effect of head diameter. Journal of Biomechanics 42(7) 912-918 (2009)

[23] Teoh S.H., Chan W.H., Thampuran R., An elasto-plastic finite element model for polyethylene wear in total hip arthroplasty. J. Biomech. 35(3) 323–330 (2002)

[24] Hegadekatte V., Huber N., Kraft O., Finite element based simulation of dry sliding wear. Modelling and Simulation in Materials Science and Engineering, 13, 57-75 (2005)

[25] Sfantos, G.K., Aliabadi, M.H.: Total hip arthroplasty wear simulation using the boundary element method. J. Biomech. 40, 378–389 (2007)

[26] Kang L., Galvin A.L., Jin Z., Fisher J., A simple fully integrated contact-coupled wear prediction for ultra-high molecular weight polyethylene hip implants. Proceedings of the Institution of Mechanical Engineers, Part H, Journal of Engineering in Medicine 220, 33–46 (2006)

[27] Askari E., Flores P., Dabirrahmani D., Appleyard R., Dynamic modeling and analysis of wear in spatial hard-on-hard couple hip replacements using multibody systems methodologies. Nonlinear Dyn 2015

[28] Mukras S., Kim N.H., Sawyer W.G., Jackson D.B., Bergquist L.W., Numerical integration schemes and parallel computation for wear prediction using finite element method. Wear 266, 822-831 (2009)

[29] Askari E., Flores P., Dabirrahmani D., Appleyard R., Nonlinear vibration and dynamics of ceramic on ceramic artificial hip joints: a spatial multibody modelling. Nonlinear Dyn. 76, 1365-1377 (2014)

[30] Archard J.F.: Contact and rubbing of flat surfaces. J. Appl. Phys. 24, 981-988 (1953)

[31] Barbour P.S.M., Stone M.H., Fisher J., A hip joint simulator study using simplified loading and motion cycles generating physiological wear paths and rates. Proc. Inst. Mech. Eng. H J. Eng. Med. 213(6) 455-467 (1999)

[32] Saikko V., Calonius O., Kernen J., Effect of slide track shape on the wear of ultra-high molecular weight polyethylene in a pin-on-disk wear simulation of total hip pros thesis. J. Biomed. Mater. Res. B Appl. Biomater. 69B(2) 141-148 (2004)

[33] Ramamurti B., Bragdon C.R., O'Connor D.O., Lowenstein J.D., Jasty M., Estok D.M., Harris W.H.: Loci of movement of selected points on the femoral head during normal gait: three-dimensional computer simulation. J. Arthoplasty 11(7) 845-852 (1996)

[34] Saikko, V., Calonius, O.: Slide track analysis of the relative motion between femoral head and acetabular cup in walking and hip simulator. J. Biomech. 35(4) 455-464 (2002)

[35] Jourdan, F., Samida, A.: An implicit numerical method for wear modelling applied to a hip joint prosthesis problem. Comput. Methods Appl. Mech. Eng. 198, 2209-2217 (2009)

[36] Askari E., Flores P., Dabirrahmani D., Appleyard R., Wear prediction of ceramicon-ceramic artificial hip joints. In: Flores P, Viadero F, editors. New trends in mechanism and machine science, from fundamentals to industrial applications. Springer; 2015.

[37] Scholes, S.C., Unsworth, A., Goldsmith, A.A.J.: A frictional study of total hip joint replacements. Phys. Med. Biol. 45, 3721-3735 (2000)

[38] Chan, F.W., Bobyn, J.D., Medley, J.B., Krygier, J.J., Tanzer, M.: The Otto Aufranc Award. Wear and lubrication of metalon-metal hip implants. Clin. Orthop. Rel. Res. 369, 10-24 (1999)

[39] Essner, A., Sutton, K., Wang, A.: Hip simulator wear comparison of metal-on-metal, ceramic-on-ceramic and cross-linked UHMWPE bearings. Wear 259(7-12) 992-995 (2005)

[40] Wang A., Sun D.C., Yau S.S., Edwards B., Sokol M., Essner A., et al. Orientation softening in the deformation and wear of ultra-high molecular weight polyethylene. Wear 203–204, 230–241 (1997)

[41] Wang A., Essner A., Polineni V. K., Stark C., Dumbleton J. H., Lubrication and wear of ultrahigh molecular weight polyethylene in total joint replacements. Tribology International 31(1-3) 17-33 (1998)

[42] Wang, A. A unified theory of wear for ultra-high molecular weight polyethylene in multi-directional sliding. Wear 248 (1-2), 38-47 (2001)

[43] Lee, K.Y., Pienkowski, D., Compressive creep characteristics of extruded ultrahigh-molecular-weight polyethylene. Journal of Biomedical Materials Research 39, 261-265 (1998)

[44] Ramamurti, B., Estok, D.M., Bragdon, C.R., Weinberg, E.A., Jasty, M., Harris, W.H., 1999. Dimensional changes in metal-backed polyethylene acetabular cups under cyclic loading. In Proceedings of the 45th annual meeting of the Orthopedic Research Society, Anaheim, CA.

[45] Davidson J. A., Schwartz G., Wear, creep, and frictional heat of femoral implant articulating surfaces and the effect on long-term performance-Part I, review, J. Biomed. Mater. Res., 21, 261-285 (1987)

[46] Askari, E., Flores, P., Dabirrahmani, D., Appleyard, R.: Study of the friction-induced vibration and contact mechanics of artificial hip joints. Tribol. Int. 70, 1-10 (2014)

[47] Flores, P., Lankarani, H.M., Spatial rigid-multi-body systems with lubricated spherical clearance joints: modeling and simulation. Nonlinear Dyn. 60, 99-114 (2010)

[48] Flores, P., Ambrósio, J., Claro, J.C.P., Lankarani, H.M.: Spatial revolute joints with clearance for dynamic analysis of multibody systems. Proc. Inst. Mech. Eng. K J. Multi-body Dyn. 220(4), 257-271 (2006)

[49] Flores, P., Ambrosio, J., Claro, J.C.P., Lankarani, H.M.: Dynamics of multibody systems with spherical clearance joints. J. Comput. Nonlinear Dyn. 1, 240-247 (2006)

[50] Bartel D.L., Burstein A.H., Toda M.D., Edwards D.L., The effect of conformity and plastic thickness on contact stress in metal-backed plastic implants. Trans. ASME, J. Biomech. Eng 107, 193-199 (1985)

[51] Di Puccio, F., Mattei, L., Biotribology of artificial hip joints. World J Orthop 6(1) 77-94 (2015)

[52] Mukras S., Kim N.H., Mauntler N.A., Schmitz T., Sawyer W.G. Comparison between elastic foundation and contact force models in wear analysis of planar multibody system. Journal of Tribology132 (3) (2010)

[53] Põdra, P., Andersson, S., Wear simulation with the Winkler surface model. Wear 207, 79-85 (1997)

[54] Johnson, K. L., 1985, Contact Mechanics, Cambridge University Press, Cambridge.

[55] Li, G., Sakamoto, M., and Chao, E. Y. S., A Comparison of Different Methods in Predicting Static Pressure Distribution in Articulating Joints. J. Biomech., 30, 635–638 (1997)

[56] Bei, Y., Fregly, B. J., Multibody Dynamic Simulation of Knee Contact Mechanics, Med. Eng. Phys., 26, 777-789 (2004)

[57] An K.N., Himenso S., Tsumura H., Kawai T., Chao E.Y.S., Pressure distribution on articular surfaces: application to joint stability analysis. Journal of Biomechanics 23 (1990) 1013–20.

[58] K.H. Hunt, F.R.E. Crossley, Coefficient of restitution interpreted as damping in vibroimpact, J. Appl. Mech. 7 (1975) 440-445.

[59] Gilardi G., Sharf I., Literature survey of contact dynamics modelling. Mechanism and Machine Theory 37, 1213–1239 (2002)

[60] Machado, M., Flores, P., Ambrósio, J., Completo, A.: Influence of the contact model on the dynamic response of the human knee joint. Proc. Inst. Mech. Eng. K J. Multi-body Dyn. 225(4), 344-358 (2011)

[61] Alves J., Peixinho N., Tavares da Silva M., Flores P., Lankarani H.M., A comparative study of the viscoelastic constitutive models for frictionless contact interfaces in solids. Mechanism and Machine Theory 85, 172–188 (2015)

[62] Gonthier Y., McPhee J., Lange C., Piedboeuf J.C., A regularized contact model with asymmetric damping and dwell-time dependent friction. Multibody Syst. Dyn. 11, 209–233 (2004)

[63] Zhang Y., Sharf I., Compliant force modeling for impact analysis, Proceedings of the 2004 ASME International Design Technical Conferences, Salt Lake City, Paper No. DETC2004–572202004.

[64] Flores, P., Machado, M., Silva, M.T., Martins, J.M.: On the continuous contact force models for soft materials in multibody dynamics. Multibody Syst. Dyn. 25(3), 357–375 (2011)

[65] Tian, Q., Flores, P., Lankarani, H.M. A comprehensive survey of the analytical, numerical and experimental methodologies for dynamics of multibody mechanical systems with clearance or imperfect joints. Mechanism and Machine Theory. 122, 1-57 (2018)

[66] Koshy, C.S., Flores, P., Lankarani, H.M.: Study of the effect of contact force model on the dynamic response of mechanical systems with dry clearance joints: computational and experimental approaches. Nonlinear Dyn. 73(1–2), 325–338 (2013)

[67] Tian, Q., Zhang, Y., Chen, L., Flores, P.: Dynamics of spatial flexible multibody systems with clearance and lubricated spherical joints. Comput. Struct. 87(13-14), 913-929 (2009)

[68] Ambrosio, J.: Rigid and flexible multibody dynamics tools for the simulation of systems subjected to con-tact and impact conditions. Eur. J. Solids A/Solids 19, S23-44 (2000)

[69] Askari, E., Flores, P., Dabirrahmani, D., Appleyard, R., A computational analysis of squeaking hip prostheses. ASME J. Comput. Nonlinear Dyn. 10(2) (2015)

[70] Atkinson, K.A.: An Introduction to Numerical Analysis, 2nd edition. Wiley, New York (1989).

[71] Braunovic, M., Konchits, V.V., Myshkin, N.K., Electrical contacts: Fundamental, applications and technology, Boca Raton Taylor & Francis (2006).

[72] Flores, P., Modeling and simulation of wear in revolute clearance joints in multibody systems, Mechanism and Machine Theory, 44, 1211-1222 (2009)

[73] Khonsari, M.K., Booser, E.R. Applied Tribology: Bearing design and lubrication. Wiley, 2017.

[74] Gill H.S., Waite J.C., Short A., Kellett C.F., Price A., Murray D.W., In vivo measurement of volumetric wear of a total knee replacement. The Knee 13, 312-317 (2006).

[75] Allen M.J., Hartmann S.M., Sacks J.M., Calabrese J., Brown P.R., Technical feasibility and precision of radiostereometric analysis as an outcome measure in canine cemented total hip replacement. J Orthop Sci 9(1), 66-75 (2004).

[76] Askari E., Flores P., Dabirrahmani D., Appleyard R., Dynamic modeling and analysis of wear in artificial hip articulations. 2015 IFToMM World Congress Proceedings.

[77] Hamilton, M.A., Sucec, M.C., Fregly, B.J., Banks, S.A., Sawyer, W.G., 2005. Quantifying multidirectional sliding motions in total knee replacements. Journal of Tribology 127, 280–286.

[78] American Academy of Orthopaedic Surgeons, AAOS, http://orthoinfo.aaos.org/topic.cfm?topic=a00377 [accessed 20.07.2017]

[79] Fregly, B.J., Sawyer, W.G., Harman, M.K., Banks, S.A., Computational wear prediction of a total knee replacement from in vivo kinematics. Journal of Biomechanics 28, 305–314 (2005)

[80] Bergmann, G., Deuretzbacher, G., Heller, M., Graichen, F., Rohlmann, A., Strauss, J., Duda, G.N: Hip contact forces and gait patterns from routine activities. Journal of Biomechanics, 34(7) 859-871 (2001)

[81] Gao Y., Jin Z., Wang L., Wang M., Finite element analysis of sliding distance and contact mechanics of hip implant under dynamic walking conditions. Proc IMechE Part H: J Engineering in Medicine 229(6) 469–474 (2015)

[82] Kang L., Galvin A.L., Jin Z., et al. A simple fully integrated contact-coupled wear prediction for ultra-high molecular weight polyethylene hip implants. ProcIMechE, Part H: J Engineering in Medicine 220, 33-46 (2006)

[83] Livermore J., Ilstrup D., Morrey B., Effect of femoral head size on wear of the polyethylene acetabular component, J. Bone Joint Surg. 72–4, 518–528 (1990)

[84] Maxian, T. A. Development and application of a finite element formulation for estimating sliding wear in total hip arthroplasty, PhD Thesis, University of Iowa, Iowa City, Iowa, USA, 1997.

[85] Atkinson J.R., Dowson D., Isaac J.H., Wroblewski B.M., Laboratory wear tests and clinical observations of the penetration of femoral heads into acetabular cups in total replacement hip joints, Wear 104, 225–244 (1985).

[86] Hall R.M., Unsworth A., Siney P., Wroblewski B.M., Wear in retrieved charnley acetabular sockets, Proc. Instn. Mech. Eng. 210, 197–207 (1996)

[87] Chen, J.H., Wu, J.S.S., Measurement of polyethylene wear-A three-dimensional methodology, Computer Methods and Programs in Biomedicine 68, 117-127 (2002)

[88] Wu, J.S.S., Hung, J.P., Shu, C.S., Chen, J.H., The computer simulation of wear behavior appearing in total hip prosthesis. Computer Methods and Programs in Biomedicine 70, 81-91 (2003)

[89] Fialho J.C., Fernandes P.R., Eca L., Folgado J. Computational hip joint simulator for wear and heat generation. Journal of Biomechanics 40(11) 2358-2366 (2007)

[90] Liu F., Fisher J., Jin Z. Effect of motion inputs on the wear prediction of artificial hip joints. Tribology International 63, 105-114 (2013)

[91] Galvin A.L., Tipper J.L., Jennings L.M., et al. Wear and biological activity of highly crosslinked polyethylene in the hip under low serum protein concentrations. Proc IMechE Part H: J Engineering in Medicine 221, 1-10 (2007)

[92] Charnley J., Halley D.K., Rate of wear in total hip replacement. Clin Orthop Relat Res 112, 170-179 (1975)

[93] Dai X., Omori H., Okumura Y., et al. Serial measurement of polyethylene wear of well-fixed cementless metalbacked acetabular component in total hip arthroplasty: an over 10 year follow-up study. Artif Organs 24, 746–751 (2000)

[94] Sychterz C.J., Engh C.A., Young A.M., Hopper R.H., Charles A., Comparison of in vivo wear between polyethylene liners articulating with ceramic and cobalt-chrome femoral heads. J Bone Joint Surg [Br] 82-B 948-951 (2000).

[95] Thomas G.E., Simpson D.J., Mehmood S., et al. The seven-year wear of highly cross-linked polyethylene in total hip arthroplasty: a double-blind, randomized controlled trial using radiostereometric analysis. J Bone Joint Surg Am 93, 716–722 (2011)

[96] Glyn-Jones S., McLardy-Smith P., Gill H. S., Murray D. W., The creep and wear of highly cross-linked polyethylene. J Bone Joint Surg [Br] 90-B 556-561 (2008)

[97] Gao L., Dowson D., Hewson R.W. Predictive wear modeling of the articulating metal-on-metal hip replacements. Journal of Biomedical Materials Research- Part B: Applied Biomaterials 105 (3) 497-506 (2017)

[98] Askari E., Jeong K.H., Amabili M. Hydroelastic vibration of circular plates immersed in a liquid-filled container with free surface. Journal of Sound and Vibration 332 (12) 3064-3085 (2013)

Figure Captions List

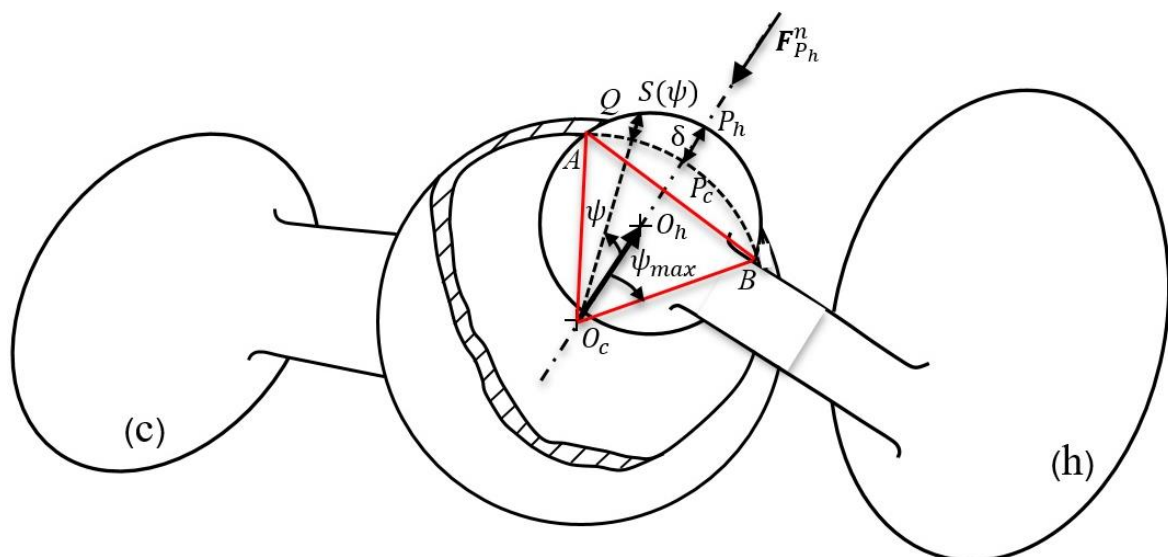Fig. 1   A general representation of the head-cup articulation.

Fig. 2   A schematic representation of contact area and penetration depth.

Fig. 3   A representation of the discretised surface of the cup in which Pc is contact point, which locates at the centre of the contact area within the circle in red colour. The green block depicts one element (k, j) engaged in the contact area.

Fig. 4   A schematic diagram of the procedure to determine the angle at which the minimum $\Im$ is found and the corresponding PMO direction is taken as the PMO direction, φ_{PMC}, [78].

Fig. 5   Physiological adopted forces with   fz (superior-inferior (SI));   fy (anterior-posterior (AP));   fx (medial-lateral (ML)) for the gait cycle.

Fig. 6   The Euler angles due to the physiological motion of the femoral head where solid line (internal-external rotation (IER)); dashed lines (abduction-adduction (AA)); dash-dotted lines α (flexion-extension (FE)).

Fig. 7   The cross-shear ratio with time and the corresponding principal molecular orientation (PMO)

Fig. 8   Top row (left to right): Logarithmic time term (minute) and average pressure distribution (Pa). Bottom row (left to right): Creep penetration (mm) and contact point trajectory projected onto the cup surface.

Fig. 9   Maximum contact pressure with time (a); accumulated sliding distance (b); Contour of wear projected onto the cup surface (c).

49

Fig. 10   Contours of creep and wear penetration (mm) for 28mm head with 8mm polyethylene liner and 0.08mm clearance. Contact point trajectory on the cup is also illustrated.

Table Caption List

Table 1   A comparison of results obtained by the current simulation with those available in the thematic literature. (hip size: 28 mm)

Table 2   A comparison of results obtained by the current simulation with those available in the thematic literature. (hip size: 22 mm)

Table 3   Total penetration of the femoral head into the polyethylene cup.

Table 4   The effect of hip implant size on predicted wear rates and creep, clearance: 80 μm and liner thickness: 8 mm

Table 5   The effect of hip implant clearance on predicted wear rates and creep, hip size: 28 mm and liner thickness: 8 mm

Figures

Fig. 1. A general representation of the head-cup articulation.

Fig. 2. A schematic representation of contact area and penetration depth.
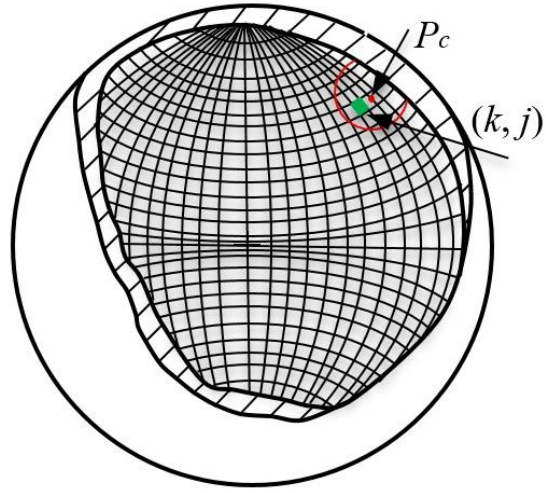
Fig. 3. A representation of the discretised surface of the cup in which P_c is contact point, which locates at the centre of the contact area within the circle in red colour. The green block depicts one element (k, j) engaged in the contact area.
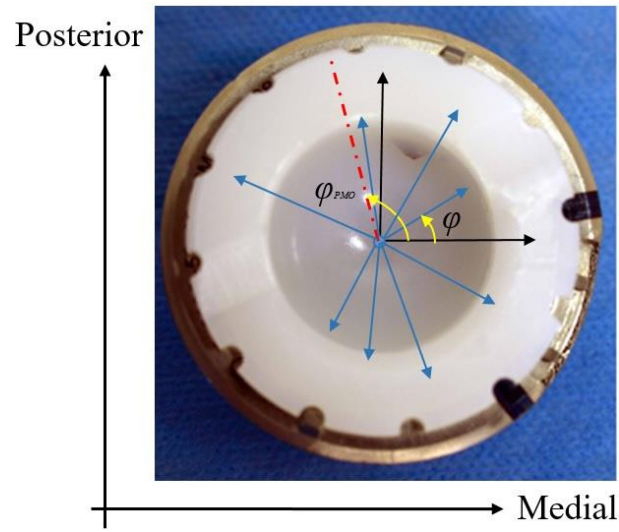
Fig. 4. A schematic diagram of the procedure to determine the angle at which the minimum $\Im$ is found and the corresponding PMO direction is taken as the PMO direction, φ_{PMC}, [78].
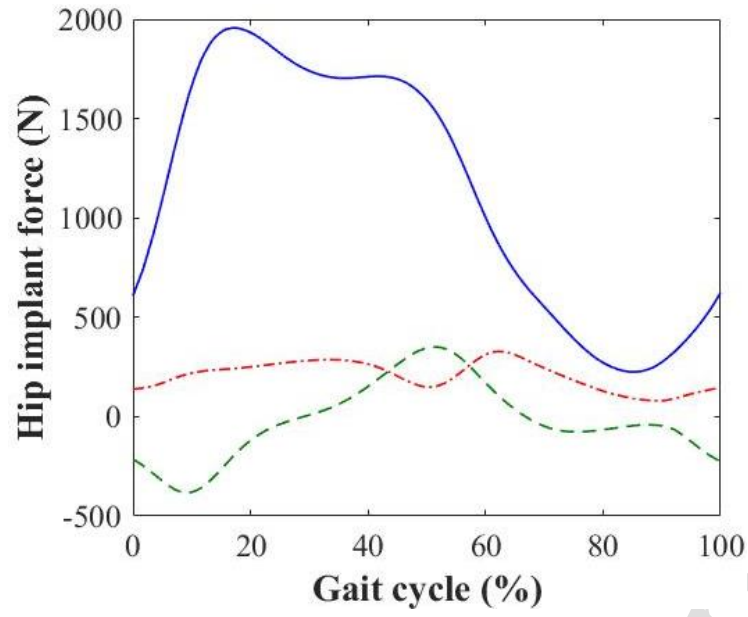
Fig. 5. Physiological adopted forces with —— f_z (superior-inferior (SI)); ---- f_y (anterior-posterior (AP)); ·-·-·- f_x (medial-lateral (ML)) for the gait cycle.
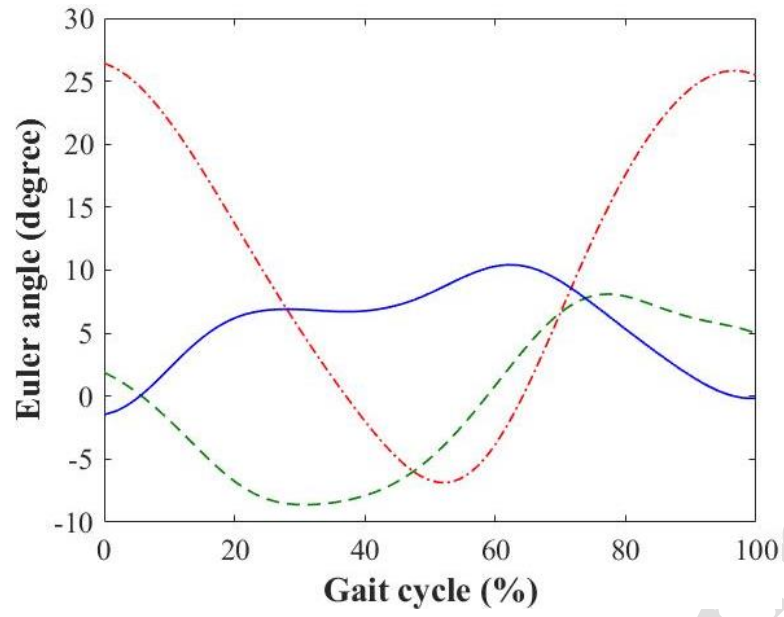
Fig. 6. The Euler angles due to the physiological motion of the femoral head where solid line (internal-external rotation (IER)); dashed lines (abduction-adduction (AA)); dash-dotted lines α (flexion-extension (FE)).
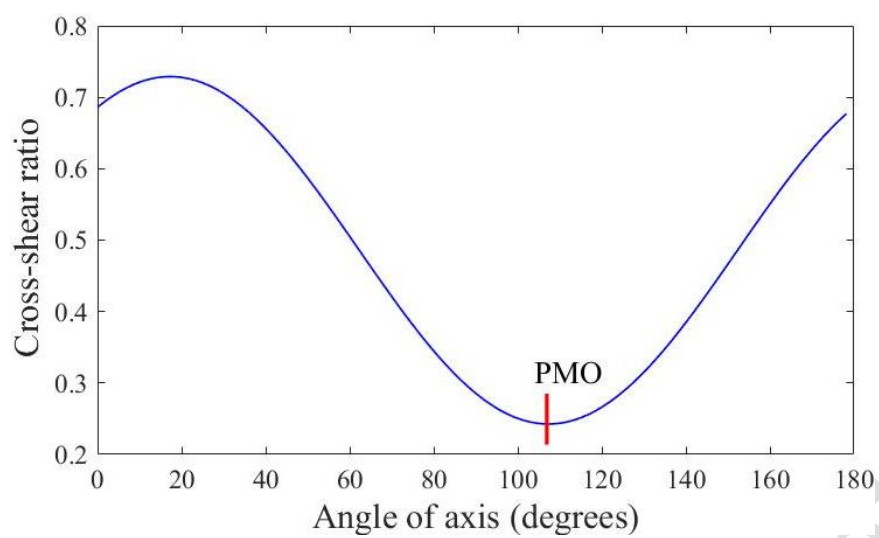
Fig. 7. The cross-shear ratio with time and the corresponding principal molecular orientation (PMO)
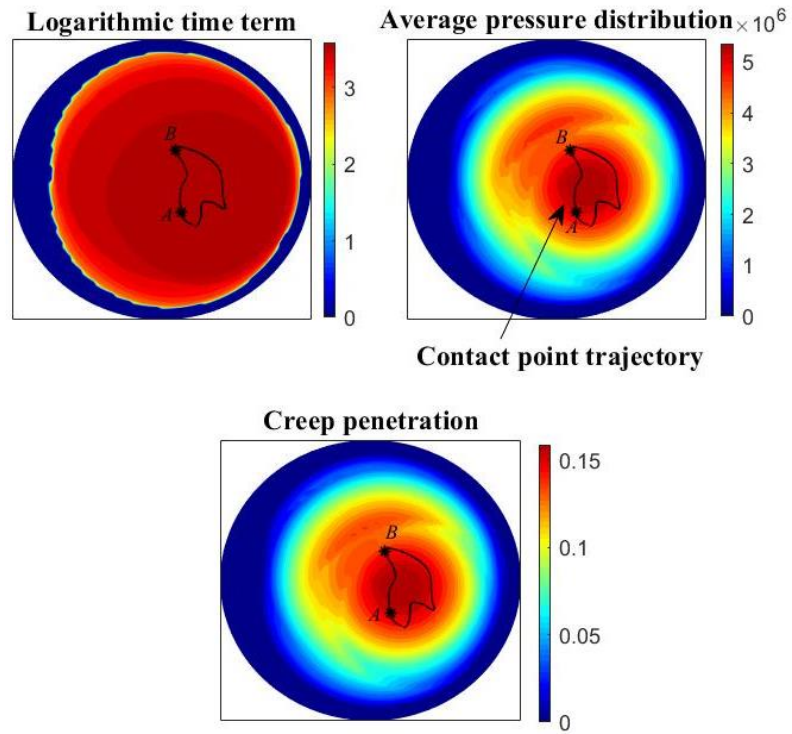
Fig. 8. Top row (left to right): Logarithmic time term (milli-minute) and average pressure distribution (Pa). Bottom row: Creep penetration (mm). Points (*A*) and (*B*) correspond to two instants of the walking cycle that are 0.1 and 0.55 s, respectively.
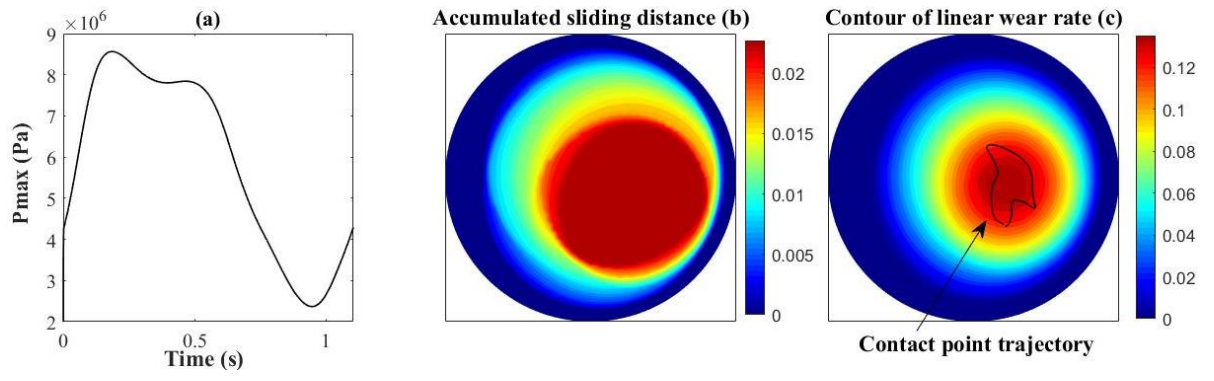
Fig. 9. Maximum contact pressure with time (a); accumulated sliding distance (b); Contour of wear projected onto the cup surface (c).
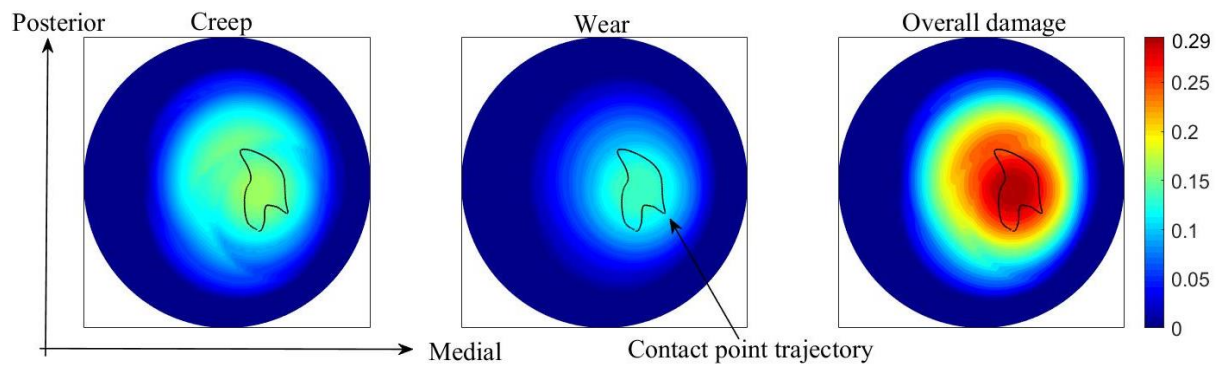
Fig. 10. Contours of creep and wear penetration (mm) for 28mm head with 8mm polyethylene liner and 0.08mm clearance. Contact point trajectory on the cup is also illustrated.

Tables

Table 1. A comparison of results obtained by the current simulation with those available in the thematic literature. (hip size: 28 mm)

Study type	Authors	Wear depth (mm/yr)	Wear volume (mm³/yr)
Clinical study	Livermore et al [83]	0-0.3 (mean: 0.08)	0-225 (mean: 48.4)
Numerical study	Maxian et al [84]	0.123	18.7
Numerical study	Kang et al [82]	0.149	22.0
Numerical study	Present model	0.135	28.3

Table 2. A comparison of results obtained by the current simulation with those available in the thematic literature. (hip size: 22 mm)

Study type	Authors	Wear depth (mm/yr)	Wear volume (mm³/yr)
Clinical study	Livermore et al [83]	0-0.39 (mean: 0.13)	0-147 (mean 47.5)
Clinical study	Atkinson et al [85]	0.005-0.623 (mean 0.19)	1.9-237 (mean: 74)
Clinical study	Hall et al [86]	0.1-0.15	----
Clinical study	Chen and Wu [87]	0.15	48.9-66.4
Numerical study	Maxian et al [84]	0.121	15.3
Numerical study	Kang et al [82]	0.163	19.7
Numerical study	Wu et al [88]	0.11	42
Numerical study	Present model	0.151	22.29

Table 3. Total penetration of the femoral head into the polyethylene cup.

Study type	authors	Overall damage (mm/yr)
Clinical study	Sychterz et al [94]	3.44
Clinical study	Thomas et al [995]	3.18
Clinical study	Glyn-Jones et al [96]	3.24
Numerical study	Present model	3.04

Table 4. The effect of hip implant size on predicted wear rates and creep, clearance: 80 μm and liner thickness: 8 mm

Cup diameter (mm)	Linear wear rate (mm/year)		Volumetric wear rate (mm³/year)		Linear creep (mm/year)
	Eq. (32)	Eq. (33)	Eq. (32)	Eq. (33)	
22	0.15124	0.0307	22.287	7.40	0.22879
28	0.13538	0.0439	28.332	15.37	0.1616
32	0.1328	0.0531	33.29	21.55	0.13462
36	0.12429	0.0611	36.402	27.53	0.115

Table 5. The effect of hip implant clearance on predicted wear rates and creep, hip size: 28 mm and liner thickness: 8 mm

Clearance (µm)	Linear wear rate (mm/year)		Volumetric wear rate (mm³/year)		Linear creep (mm/year)
	Eq. (32)	Eq. (33)	Eq. (32)	Eq. (33)	
20	0.08516	0.0425	28.37	23.23	0.10158
40	0.10681	0.0433	28.478	19.51	0.12663
80	0.13538	0.0439	28.332	15.37	0.1616
100	0.14853	0.0440	28.543	13.99	0.1753
200	0.19019	0.0465	28.365	10.08	0.23454